

Mitochondrial hTERT rewires glucose metabolism to confer cancer chemoresistance by binding to MT-ND1

Xinzhe Li

Army Medical University

Xing Chang

Army Medical University

Weichao Hu

Army Medical University

Yongbing Zhao

Army Medical University

Zhengguo Xu

Army Medical University

Mengyuan Gao

Army Medical University

Qin Ouyang

Army Medical University <https://orcid.org/0000-0002-1161-5102>

Shengwei Zhang

Army Medical University

Qingyun Tang

Army Medical University

Junjian He

Army Medical University

Liting Wang

Third Military Medical University

Xianlong Ling

Army Medical University

Shiming Yang

Army Medical University

Changjiang Hu (✉ hcj888@tmmu.edu.cn)

Army Medical University

Keywords: hTERT, Glucose metabolism, Chemoresistance, Mitochondrial Complex I, MT-ND1

Posted Date: March 2nd, 2022

DOI: <https://doi.org/10.21203/rs.3.rs-1342028/v1>

License:   This work is licensed under a Creative Commons Attribution 4.0 International License.

[Read Full License](#)

Abstract

Resistance to chemotherapy represents a bottleneck in clinical cancer treatment and demands urgent solutions. Dysfunction of glucose metabolism including the Warburg effect is an outstanding hallmark of aberrant cancer metabolism which remarkably fosters chemoresistance. Targeting disordered mitochondrial metabolism have paved the road for enhancing chemosensitivity. Human telomerase reverse transcriptase (hTERT) is tightly associated with cancer initiation and progression. Notably, hTERT can unconventionally translocate from nucleus to mitochondria. However, the influence of mitochondrial hTERT on glucose metabolism and the subsequent contribution to chemoresistance remains largely elusive. Here, we uncovered that mitochondrial hTERT level is negatively with chemotherapy response in patients, and disclosed the undocumented role of mitochondrial hTERT in reprogramming cancer metabolism towards Warburg effect independent of RT activity which authentically promoted chemoresistance. Mitochondrial hTERT boosted Warburg effect and weakened oxidative phosphorylation (OXPHOS) specifically via suppressing Complex I activity. Interactome profiling by mass spectrometry revealed that mitochondrial hTERT physically interacted with Complex I core subunit MT-ND1 (ND1) through its matrix loop region to hinder Complex I functions. A novel TAT-Pep designed on the basis of their interacting region effectively abrogated the hTERT-ND1 interplay, which substantially rejuvenated Complex I activity and rewired cancer metabolism from Warburg effect towards OXPHOS thereby strengthening chemosensitivity in both resistant cancer lines and patient-derived xenograft (PDX) tumor models. Collectively, our study reveals the interaction between MT-ND1 and hTERT as an essential mechanism that underlies the rewiring of cellular glucose metabolism and chemoresistance. Targeting mitochondrial hTERT-governed adverse metabolic remodeling sheds light on the avenue towards better chemotherapeutics efficacy.

Background

Although targeted cancer therapy and immunotherapy have shown inspiring results in clinical trials, traditional chemotherapy regimen including cisplatin (CDDP) and platinum-based drugs remains a therapeutic cornerstone in large varieties of solid tumors¹⁻⁵. However, many patients become refractory to chemotherapy treatment after an initial therapeutic response, which represents a challenging issue. The intrinsic or acquired resistance to chemotherapy are traditionally driven by various mechanisms⁶⁻⁸. One of the emerging noteworthy reasons for chemoresistance is aberrant mitochondria metabolism, which is recognized as a prominent hallmark of cancer. Normal cells prefer to utilize oxidative phosphorylation (OXPHOS) over glycolysis to generate more ATP in sufficient oxygen conditions. However, cancer cells are featured by enhanced glycolysis. Even under aerobic conditions, the rapidly-proliferating cancer cells are inclined to use glycolysis rather than OXPHOS. This paradoxical glucose metabolism was firstly observed by Otto Warburg⁹⁻¹¹. The Warburg effect boosts glucose consumption and lactate production much more than normal cells, which facilitates tumors to transform abundant carbon sources towards lactate and generate biosynthetic intermediates as precursors for highly-motivated anabolic processes. Excessive lactate production favors a pro-tumorigenic microenvironment

which endows tumor growth, metastasis and further contributes to therapy resistance. Besides, the lowered mitochondrial OXPHOS impairs reactive oxygen species (ROS)-induced toxicity to protect cancer cells from death⁹⁻¹¹. The Warburg effect drives chemoresistance with different mechanisms, including promoting epithelial-mesenchymal transition (EMT), enhancing cancer stemness, accelerating drug efflux, raising DNA damage repair, facilitating immune evasion, et al¹²⁻¹⁴. Therefore, targeting Warburg effect emerges as a promising strategy to enhance chemosensitivity.

Telomerase is closely related with approximately the whole properties of cancers. Human telomerase reverse transcriptase (hTERT) is the catalytic subunit of human telomerase whose canonical function is to maintain chromosomal integrity and genome stability in nucleus. Dysregulation of hTERT abundance or activity leads to aberrant telomerase activation, which promotes cancer progression and chemoresistance¹⁵⁻¹⁸. Conventionally, the reverse transcriptase (RT) activity is critical for hTERT to promote cancer growth and survival^{15,19}. Recently, the non-classical roles of hTERT have also aroused wide attentions^{20,21}. Our group have also shown that hTERT formed complex with MDM2 to finally increase ITGB1 levels thus promoting gastric cancer cells invasion²². Notably, hTERT can translocate from nucleus into mitochondria with the guidance of the N-terminal mitochondrial targeting sequence (MTS) to act in a non-canonical manner²³. Effects of mitochondria-translocated hTERT on cellular function are controversial in different studies. Several groups reveal that mitochondria-localized hTERT improved mitochondrial function by alleviating ROS to heighten cellular antioxidant defense, which protects cancer cells from oxidative stress-associated damage²⁴⁻²⁷. Absence of hTERT in mitochondria negatively impacts the organelle by increasing mtDNA damage and ROS production relying on its RT activity²⁸. On the contrary, other groups proposes that hTERT mitochondrial localization makes cells more vulnerable to oxidative stress-induced mtDNA toxicity which enhances cell death^{23,29}.

Similarly, the contemporary paradigm for the role of hTERT mitochondrial localization in cancer therapy is also confined to the available evidences that hTERT translocates from the nucleus to the mitochondria, reduces ROS production and relieves the oxidative stress to mtDNA³⁰⁻³² or nuclear DNA³³, which protects cancer cells from apoptosis. However, it has not been validated whether the mitochondrial hTERT authentically promotes chemoresistance, or they are merely paralleled rather than causally associated. Notably, as mitochondria is the hub of cellular metabolism, it still remains largely unknown if mitochondrial hTERT is able to induce the distinctive cancer metabolism phenotype such as the Warburg effect. Most importantly, the impact of hTERT-mediated metabolic rewiring on therapeutic resistance and corresponding targeted strategy is yet to be clarified. In this study, we aimed to address the above issues.

Results

Mitochondrial hTERT negatively influences cancer response to chemotherapy.

To identify the association between mitochondrial hTERT and chemotherapeutic effect, various CDDP-resistant cancer cell models (HCC, colorectal cancer, gastric cancer and lung cancer) were generated

(Figure 1A). Results clearly demonstrated that mitochondrial hTERT was remarkably elevated in CDDP-resistant cancer cells compared to their parental cells (Figure 1B-C). Next, we further inquired the relevance between mitochondrial hTERT and chemotherapy response of HCC patients (Table S1). As shown in Figure 1D, mitochondrial hTERT was much more in Case 2 and Case 3 compared to that in Case 5 and Case 7. These patients subsequently underwent standard interventional operations (Transcatheter Arterial Chemoembolization, TACE) with platinum drugs. Therapeutic effects were evaluated by reduction of tumor areas and Alpha Fetoprotein (AFP) levels before and after TACE (within 3 months). Both tumor sizes and AFP levels decreased more dramatically in Case 5 and 7 than those in Case 2 and Case 3 (Figure 1E-G), which strongly revealed that increased mitochondrial hTERT levels impeded anticancer therapeutics. We further excavated clinical data from the Cancer Genome Atlas (TCGA) database and found that although hTERT was highly expressed in HCC tissues compared to its adjacent para-tumor tissues (Figure S1A), there was no significant difference of hTERT levels between the therapy-sensitive and therapy-resistant groups (Figure S1B-C). Besides, the receiver operating characteristic (ROC) curve analysis of hTERT-based drug response prediction (Figure S1D) and survival prediction (Figure S1E), and the Cox Regression (Figure S1F) all indicated that total hTERT was not able to effectively predict treatment response or survival rate. The above clinical characteristics suggested that the underlying mechanism for hTERT-mediated chemotherapy resistance may be related to the changed subcellular location. Taken together, mitochondrial hTERT negatively influence response to chemotherapy in both chemotherapy-resistant cancer cells and HCC patients.

Mitochondrial hTERT rewires cellular glucose metabolism and confers chemoresistance in a telomerase RT independent manner.

To further investigate whether mitochondrial hTERT could promote chemoresistance and reshape cancer metabolism independent of its classical RT activity, we established the following cell models: ^{WT}hTERT (overexpressing wild-type hTERT), ^{DN}hTERT (mutation of RT activity) and ^{NUC}hTERT (mutation of hTERT MTS based on ^{DN}hTERT) (Figure 2A). Telomeric repeat amplification protocol (TRAP) assays verified that ^{DN}hTERT lacked the RT activity (Figure 2B). In addition, mitochondria-located hTERT in ^{NUC}hTERT cells was much diminished than that in ^{WT}hTERT and ^{DN}hTERT cells (Figure 2C-D and Figure S2A). Both ^{WT}hTERT and ^{DN}hTERT cells were resistant to CDDP compared to Control cells (Figure 2E). Importantly, ^{NUC}hTERT cells regained sensitivity to CDDP compared with the ^{DN}hTERT cells. These data indicated mitochondrial hTERT conferred chemotherapy resistance independent of RT activity (Figure 2E). Next, we explored how mitochondrial hTERT reprogrammed cancer metabolic phenotype. Using the mitochondria stress assay, the oxygen consumption rate (OCR) (Figure 2F) and maximal respiration (Figure 2G) were analyzed to profile mitochondrial respiration. Both of them were blunted in ^{DN}hTERT cells compared to Control cells, while they were substantially restored in ^{NUC}hTERT cells. Besides, the glycolytic stress assay was utilized to indicate levels of lactic acid fermentation by measuring the extracellular acidification rate (ECAR) (Figure 2H) and glycolytic capacity (Figure 2I). Results showed ^{DN}hTERT cells enhanced both of them, which were obviously downregulated in ^{NUC}hTERT cells. Warburg effect is characterized by boosted glucose consumption and L-lactate production. Then these metabolic materials or products were

examined. Glucose (Figure 2J) and ATP levels (Figure S2B) were decreased in ^{DN}hTERT cells, while they were elevated in ^{NUC}hTERT cells compared with ^{DN}hTERT cells. Meanwhile, ^{DN}hTERT cells generated more L-lactate than Control cells. However, L-lactate production was markedly reduced in ^{NUC}hTERT cells compared to ^{DN}hTERT cells (Figure 2K). Collectively, the enhancement of OXPHOS and reduction of lactic acid fermentation by ^{NUC}hTERT undoubtedly demonstrated that mitochondria hTERT promoted Warburg effect. Warburg effect could support chemoresistance in multiply avenues, including facilitating epithelial-mesenchymal transition (EMT) process and favoring cancer stemness¹²⁻¹⁴. Consistent with that, ^{DN}hTERT increased the protein levels of EMT markers (N-Cadherin, ZEB1 and Snail) and cancer stemness markers (OCT4 and Nanog), while ^{NUC}hTERT decreased them compared to ^{DN}hTERT (Figure S2C-D). In conclusion, the mitochondrial hTERT, independent of RT activity, induced aerobic glycolysis-dominated metabolic rewiring and drove chemotherapy resistance.

hTERT reprograms mitochondrial metabolism via inhibiting Complex I activity.

There are 5 respiratory chain complexes in human mitochondria, which coordinate together to govern a series of redox processes and dominate OXPHOS. Dysfunction of cancer respiratory chain complexes impairs OXPHOS and facilitates glycolytic metabolic profile to expedite chemoresistance³⁴. Figure S3A-E showed that only Complex I activity was significantly reduced in ^{DN}hTERT cells compared to Control cells. In addition, the repressed Complex I activity in ^{DN}hTERT cells could be dramatically improved in ^{NUC}hTERT cells (Figure 3A). Complex I is the largest and most complicated enzyme among mitochondrial respiratory chains which transfers electrons from nicotinamide adenine dinucleotide (NADH) to the electron transport chain (ETC) for ATP synthesis. During this process, the reductive NADH derived from tricarboxylic acid (TCA) cycle is oxidated to NAD⁺, and the deficiency in Complex I function will change levels of NAD⁺ and/or NADH^{35,36}. As was shown, ^{DN}hTERT decreased the levels of NAD⁺ and the ratio of NAD⁺/NADH, while ^{NUC}hTERT increased both of them compared to ^{DN}hTERT (Figure 3B and Figure S3F). To validate whether mitochondrial hTERT elicited Warburg effect exactly through suppressing Complex I activity, we introduced the yeast single subunit NADH-ubiquinone oxidoreductase Ndi1, which is acknowledged to restore human Complex I function^{37,38}. Ectopically overexpressing Ndi1 significantly enhanced Complex I activity in ^{DN}hTERT cells (Figure 3C). Besides, Ndi1 supplementation increased ^{DN}hTERT-attenuated OCR (Figure 3D) and maximal respiration (Figure 3F) levels. In addition, Ndi1 overexpression decreased ^{DN}hTERT-induced ECAR (Figure 3E) and glycolytic capacity (Figure 3G) levels. Likewise, while ATP production was reduced by ^{DN}hTERT, it was rescued by Ndi1 (Figure S3G). These results suggested that mitochondrial hTERT promoted glycolysis and inhibited OXPHOS via suppressing Complex I activity. In parallel with the above findings, rescuing Complex I activity by Ndi1 significantly abated chemoresistance of ^{DN}hTERT cells to CDDP (Figure 3H). Taken together, mitochondrial hTERT reshaped a glycolytic-characterized metabolism to render chemoresistance via inhibiting Complex I activity.

Mitochondrial hTERT physically interacts with the Complex I subunit MT-ND1.

Mitochondria Complex I plays central roles in OXPHOS. It consists of 45 highly conserved subunits (7 mitochondria-encoded and 38 nucleus-encoded) essential for electron transfer and generating proton gradient³⁹. To figure out which component of Complex I was closely involved in mitochondrial hTERT-mediated metabolic remodeling, unbiased mass spectrometry screening combined with subsequent co-immunoprecipitation (Co-IP) assays were performed. Results showed that mitochondria DNA-encoded subunit NADH-ubiquinone oxidoreductase chain 1 (MT-ND1, hereinafter ND1), NADH-ubiquinone oxidoreductase chain 5 (MT-ND5, hereinafter ND5) and nucleus DNA-encoded subunit NADH dehydrogenase (ubiquinone) flavoprotein 2 (NDUFV2) may potentially interact with hTERT (Table S2). Co-IP further demonstrated that only ND1 interacted with hTERT (Figure 4A). Similarly, only ND1 and hTERT could be pulled down reciprocally in endogenous hTERT-negative osteosarcoma U2OS cell models (Figure 4B). In addition, immunofluorescence revealed ^{DN}hTERT colocalized with ND1 in mitochondria while the colocalization was dramatically diminished in ^{NUC}hTERT cells (Figure 4C-D). Furthermore, Z-Dock prediction illustrated potential binding sites between hTERT and ND1 (Figure 4E-F). ND1 serves as one of the Complex I core subunits uniquely distributed in mitochondria which plays crucial roles in electron transfer and proton pumping³⁹. It is a 8 transmembrane protein that inserts into the inner mitochondrial membrane and forms 4 loop regions facing mitochondrial matrix (Figure 4G). Molecular Docking predicted the potential interacting regions between ND1 and hTERT within the ND1 protein. Then the corresponding deletion mutations were designed to explore which region was pivotal for the mitochondrial hTERT-ND1 interaction (Figure 4H). Results showed that only when Region 5 was deleted, the association between ND1 and hTERT was greatly abrogated (Figure 4H), indicating that Region 5 was critical for the interaction between mitochondrial hTERT and ND1. Taken together, mitochondrial hTERT physically interacted with the Complex I core subunit ND1, which may disturbed Complex I-mediated OXPHOS and facilitated aerobic glycolysis.

Blocking interaction between hTERT and ND1 by a novel TAT-Pep enhances chemosensitivity by weakening Warburg effect.

To investigate whether the Region 5-based hTERT/ND1 interaction was essential for mitochondrial hTERT-mediated metabolic reshaping and chemotherapy resistance, we designed an original blocking peptide aiming to abate their association. Noticeably, the amino acid sequences of Region 5 (FMAEY) across different species were highly conserved (Figure S4A). We accordingly designed a peptide (sequence GPFALFFMAEYT, hereinafter Pep) on the basis of Region 5 sequence (Figure 5A). Pep reduced the hTERT/ND1 interaction *in vitro* using lysates of HA-ND1-overexpressed ^{DN}hTERT cells (Figure S4B). To further abrogate the interaction between hTERT and ND1 *in vivo*, a TAT-leading cell-penetrating peptide (sequence YGRKKRRQRRR-GPFALFFMAEYT, hereinafter TAT-Pep) was constructed (Figure 5A). Immunofluorescence showed TAT-Pep effectively localized into mitochondria (Figure 5B). Besides, there was no obvious toxicity using TAT-Pep alone (Figure S4C). In addition, Co-IP assay revealed that the interaction between hTERT and ND1 was dramatically diminished by TAT-Pep (Figure 5C). Next, we interrogated whether blocking interaction between hTERT and ND1 by TAT-Pep could reverse the reprogrammed mitochondrial metabolism. TAT-Pep remarkably boosted Complex I activity (Figure 5D),

heightened levels of NAD⁺ (Figure 5E) and NAD⁺/NADH ratio (Figure S4D), and enhanced ROS generation (Figure S4E) and ATP production (Figure S4F). Besides, Levels of OCR (Figure 5F) and the maximal respiration (Figure 5G) were significantly enhanced by TAT-Pep. In parallel with the results in ^{DN}hTERT cells, TAT-Pep also increased NAD⁺ levels and NAD⁺/NADH ratio (Figure S4I-J), upregulated ROS generation and ATP production (Figure S4K-L) in endogenous CDDP-resistant cancer cells. These data demonstrated that TAT-Pep revitalized the mitochondrial hTERT-mediated OXPHOS inhibition. In accordance with these findings, TAT-Pep also considerably attenuated levels of ECAR (Figure 5H) and glycolytic capacity (Figure 5I). In addition, glucose consumption (Figure 5J) and lactate production (Figure 5K) were also simultaneously reduced by TAT-Pep. Moreover, TAT-Pep remarkably downregulated levels of the EMT (Figure S4G and S4M) and cancer stemness (Figure S4H and S4N) markers, which ultimately recovered the chemotherapeutic effect (Figure 5L-M). Collectively, interfering with the hTERT/ND1 interplay redirected mitochondrial hTERT-induced Warburg effect to OXPHOS, which substantially overcame chemoresistance.

Disrupting the hTERT/ND1 interaction enhances therapeutic effects of CDDP in PDX tumor models.

To validate the sensitizing effect of hTERT/ND1 interaction blockage in clinically relevant animal models, we established the patient-derived xenograft (PDX) tumor mice models using the HCC samples (Table S3). Mitochondrial hTERT level was lower in Sample 29 while it was relatively higher in Sample 35 (Figure 6A). Then the PDX models derived from Sample 29 were treated with CDDP, meanwhile those derived from Sample 35 were treated with CDDP, TAT-Pep or the combination of TAT-Pep with CDDP. Results showed that CDDP treatment dramatically decreased tumor volumes of Sample 29. In contrast, PDX tumors of Sample 35 were less sensitive to CDDP administration. Importantly, combinational treatment with TAT-Pep and CDDP was more potent than CDDP alone to delay tumor growth and shrink tumor volumes of Sample 35 (Figure 6B-D). Interaction between hTERT and ND1 was more remarkable in tumors of Sample 35 than that in tumors of Sample 29, and combinational treatment with TAT-pep decreased the hTERT/ND1 association in Sample 35 (Figure 6E). In addition, levels of NAD⁺ (Figure 6F) and NAD⁺/NADH ratio (Figure S5A) were less in Sample 35 compared to Sample 29, and both of them were augmented by supplementation of TAT-Pep. Moreover, the EMT (Figure S5B) and cancer stemness (Figure S5C) markers were higher in tumors of Sample 35 than Sample 29, which were decreased by TAT-Pep treatment. Taken together, disrupting the hTERT/ND1 interaction enhanced therapeutic effects of CDDP in clinically-associated PDX tumor models

Discussion

Although it has been well documented for the role of hTERT in maintaining telomerase activity, emerging studies reveals the non-classical role of hTERT to favor cancer initiation and progression by the telomeric-independent mechanism. Conspicuously, hTERT can translocate to mitochondria under stresses. However, the way mitochondrial hTERT acts on cancer metabolism and how this remodeled-metabolism influences chemotherapy remains widely unknown. In this study, we found that mitochondrial hTERT levels were elevated not only in CDDP-resistant cancer cells but also in refractory patients receiving TACE

treatment, indicating that it may serve as a biomarker of clinical chemotherapy response (Figure 1). Previous studies about hTERT-mediated influence on mitochondria are mainly confined to modulating the redox status. Few studies have been recorded to illustrate roles of mitochondrial hTERT in metabolic reprogramming. Viswanath et al. finds that hTERT expression is correlated with elevated glucose flux through the pentose phosphate pathway (PPP) and its major product NADPH. Increased NADPH maintains glutathione in a reduced state in low-grade gliomas⁴⁰. Ahmad group dictates the distinct role of hTERT in lipid reprogramming by interplaying with EZH2 in glioblastoma⁴¹. However, the relationship between mitochondrial hTERT and the prominent Warburg effect is still uncovered, which deserves further investigating. Herein, we for the first time unmasked that mitochondria-located hTERT independent of its RT activity promoted the Warburg effect. Defects in MTS remarkably abrogated the levels of ECAR, glycolic capacity, lactate secretion, and glucose consumption. Meanwhile, decreased mitochondrial hTERT significantly elevated levels of OCR, maximal respiration and generated more ATP (Figure 2). This metabolic remodeling increased markers of EMT and cancer stemness, which are recognized to promote chemoresistance. More importantly, we accurately depicted mitochondrial hTERT as one of the driving forces for chemotherapy resistance using the MTS-mutant cell models (^{NUC}hTERT versus ^{DN}hTERT) (Figure 2). These results extended the RT-independent function of hTERT, and established a undocumented link between hTERT and Warburg effect, which may provide insight into leveraging hTERT-induced metabolic vulnerability to overcome chemoresistance.

Mitochondrial Complex I is largest among the 5 macromolecular complexes in human mitochondrial OXPHOS system. It plays a central role in energy metabolism by boosting electron transport and proton motive force generation. Dysfunction of Complex I is closely related with diverse diseases. Current knowledge reveals a complicated double-edged role of Complex I in cancer initiation, progression and response to chemotherapy^{42,43}. Only scattered studies have investigated the impact of hTERT on mitochondrial Complex I in non-malignant models so far. Sahin et al. shows telomere dysfunction resulted in marked decline in complex I activity in both Tert^{-/-} and Terc^{-/-} mice models without distinguishable mitochondria profiles⁴⁴. Sherman et al. applies machine learning of large in vitro databases and they identifies that TERT expression is tightly associated with the NDUF gene family of Complex I component⁴⁵. In addition, Haendeler et al. shows that TERT increases Complex I activity in a RT-dependent manner. Interestingly, notwithstanding a significant decrease of Complex I activity is observed in heart mitochondria from TERT^{-/-} mice, there is no such difference in liver mitochondria²⁵. Recently, they further demonstrates that mitochondrial TERT enhances Complex I activity and thus protecting cardiomyocyte cells from ischemia/reperfusion injury by ameliorating the ratio between matrix arm and membrane arm of the Complex I subunits⁴⁶. However, increased mitochondrial TERT does not necessarily seem to induce tumors⁴⁶. This may be attributed to the relatively quiescent characteristic of cardiocytes. To date, the way mitochondrial hTERT regulates the Complex I function in cancer progression or chemoresistance is entirely unknown. We showed that impeding hTERT mitochondrial translocation significantly restored Complex I activity and raised the NAD⁺/NADH ratio. Besides, ectopic expression of Ndi1 to recover Complex I function dramatically attenuated the Warburg effect and

resensitized resistant cancer cells to CDDP (Figure 3). Our data were consistent with the viewpoint that a modest loss of Complex I function will promote cancer progression^{34,47}. The discrepancy of the impact of mitochondria TERT on Complex I activity between ours and others may be probably due to the totally different cell models and cellular context. In spite of distinct mechanisms, mitochondria TERT exhibits the similar cell-protection functions in both non-malignant and malignant models. Taken together, our data demonstrated that mitochondria hTERT hindered Complex I function, which contributed to the metabolic shift from OXPHOS to glycolysis and ultimately conferred chemoresistance.

Complex I consists of 38 nuclear-encoded subunits and 7 mtDNA-encoded subunits. Assembly of Complex I with these subunits is coordinated dynamic processes which is strictly orchestrated and interconnected by diversified assembly factors. Obstructing normal assembly process results in dysfunction of Complex I⁴⁸⁻⁵⁰. Leveraging an unbiased mass spectrometry followed by Co-IP, we systematically screened the potential components of Complex I that may interplay with and mediate the inhibitory function of mitochondria hTERT. Results showed that only ND1 was mutually co-precipitated with hTERT. To our knowledge, this is the first evidence that hTERT physically interacts with ND1 protein (Figure 4). ND1 is one of the evolutionally conserved core subunit which participates in the early assembly of Complex I^{48,50}. Both wild type or mutant ND1 gene is bound up with various cancers such as colorectal cancer⁵¹⁻⁵³, breast cancer⁵⁴, renal cell carcinoma⁵⁵, glioblastomas⁵⁶, and thyroid cancer⁵⁷. Mutation of ND1 gene manifests two-sided effects on tumor biology. Gasparre et al. have clarified an *Oncojanus* function of the homoplasmy of a truncating mutation in ND1 which hinders the tumorigenesis and metastasis⁵⁸. While Calabrese et al. illustrates that complementation of a truncative mutant ND1 is sufficient to perform the glycolytic shift upon hypoxia response and thereby promoting cancer progression⁵⁹. The ND1 gene mutation exhibits repressing impact on Complex I. For instance, A frame-shift mutation in the ND1 gene reduces Complex I activity^{60,61}. In addition, the m.3395A>G mutation within ND1 renders itself more susceptible to degradation and leads to reduction of both activity and quantity of Complex I. However, this mutation have no impact on quality of complex I assembly⁶². ND1 protein is tightly regulated and coordinated by several regulatory factors during assembly of Complex I. Knockdown of assembly factors NDUFAF3⁶³ or NDUFAF7⁶⁴ or suppression of NDUFAF5⁶⁵ profoundly decreases the levels of ND1 subunit. Besides, loss of ND1 protein disrupts Complex I biogenesis during early stages of assembly^{66,67}. Interestingly, Haendeler et al. have identified 2 regions containing the coding sequences of ND1 and ND2 as interaction sites with hTERT²⁵. In contrast, Sharma et al. reveals that hTERT binds to various regions of the mtDNA, including but not limited to ND1 and ND2²⁸. Yan shows that mitochondrial ND1 protein levels does not change significantly upon CDDP treatment³⁰. As protein is the ultimate functional implementer, the above studies led us to make a hypothesis that mitochondria hTERT physically interplayed with ND1 protein, which hindered the early assembly of Complex I thereby repressing its function. To ascertain the hypothesis, we further uncovered the protein sequence mediating their interaction within ND1 protein and accordingly designed a novel TAT-Pep that effectively hampered hTERT binding to ND1 (Figure 5). Importantly, blocking the hTERT/ND1 interplay significantly weakened Warburg effect phenotype and refreshed the OXPHOS. This metabolic

improvement remarkably raised chemotherapy effect in both chemoresistant cancer cells and PDX tumor models (Figure 5 and 6). These data stressed the importance of associating with Complex I core subunit ND1 in mitochondrial hTERT-elicited Warburg effect and also reinforced the crucial role of ND1 in maintaining Complex I function. However, the underlying mechanism of how hTERT translocates to mitochondria needs further investigations.

Taken together, our study deciphers the undocumented function of mitochondria hTERT in governing the metabolic rewiring towards the Warburg effect and thus conferring chemoresistance. The underlying mechanism lies in that mitochondrial hTERT interacts with the Complex I core subunit ND1 to disrupt assembly of Complex I and diminishes its activity. Targeting the hTERT/DN1 interplay by a novel TAT-Pep redirects metabolic regimen from aerobic glycolysis to OXPHOS, which improves chemotherapeutics effects in resistant cancer lines as well as PDX tumor models. Our results built a new link between hTERT and Warburg effect, which may provide insight to original translational strategies for improving chemotherapy sensitivity by targeting mitochondrial hTERT-mediated metabolic remodeling.

Methods

Cell Lines

The cell lines Huh7, HCT15, A549, U2OS and 293T were from American Type Culture Collection (ATCC, Manassas, USA). Cell line SGC7901 was from the Cell Bank of the Shanghai Institute for Biological Sciences (Chinese Academy of Sciences, Shanghai, China). Huh7 CDDP-R cell line was from Zhewen Corporation (Shanghai, China). HCT15 CDDP-R, SGC7901 CDDP-R and A549 CDDP-R cell lines were from our lab. Cell lines were authenticated by STR fingering by Biowing Applied Biotechnology Corporation (Shanghai, China) and tested for mycoplasma contamination. The cells were cultured in Dulbecco's modified Eagle's medium supplemented with 10% fetal bovine serum and 1% penicillin-streptomycin mixture (Beyotime, Shanghai, China) at 37 °C in a cell incubator with 5% CO₂.

TCGA database

The hepatocellular carcinoma (HCC) data including 50 tumor tissues and corresponding para-tumor tissues, and 28 therapy-resistant and 14 therapy-sensitive patients were extracted from the Cancer Genome Atlas (TCGA, <https://www.cancer.gov/tcga>). Then clinical characteristics including age, sex, live status, survival days and therapy response were used for further analysis.

Plasmids, lentivirus construction and transfection

The ^{WT}hTERT plasmid was constructed and inserted into the pLVX-IRES-Puro Vector with the restriction sites 5'-EcoRI and 3'-EcoRI. The ^{DN}hTERT plasmid was derived on the basis of ^{WT}hTERT by mutation of D712A and V713I. The ^{NUC}hTERT plasmid was derived on the basis of ^{DN}hTERT by mutation of R3E and R6E. Vector constructions were verified by direct sequencing and subsequent Western Blot. The plasmid for Ndi1 lentivirus was constructed using the *Saccharomyces cerevisiae* Ndi1 and inserted into the pLVX-

IRES-Neo Vector with the restriction sites 5'-XhoI and 3'-NotI. All the above plasmids were then packaged into lentivirus by Labs Biology Corporation (Chongqing, China). For lentivirus infection, cells (30%-50% confluency) were incubated with lentivirus mixed with polybrene. After 24 h, puromycin (5 mg/mL) was added to the medium to select for stable transfected Huh7 and HCT15 cells. Overexpression plasmids for HA-ND1, HA-ND2, HA-ND3, HA-ND4, HA-ND4L, HA-ND5, HA-ND6 and His-NDUFV2, the mutation plasmids of HA-ND1 (Mut1, Mut2, Mut3, Mut4, Mut5 and Mut6) were all synthesized by Youbio Cooperation (Changsha, China). For transient transfection, these plasmids were transfected into corresponding cells using lipofectamine 3000 reagent (L3000015, Invitrogen, USA) according to the manufacturer's protocol.

Human tissues

The HCC tissues of the patients who underwent a standard TACE operation were collected from **DBPR** (Patients' information listed in Table S1). The HCC tissues used in the establishment of PDX models were collected from **DBPR** (Patients' information listed in Table S3). All tissues were immediately preserved in liquid nitrogen. The informed consent was agreed by all patients. This study was approved by the Ethics Committee of **DBPR**. Tumor areas were calculated by the Software of General Electric Company.

Antibodies

The primary antibodies for Western Blot and Co-IP were hTERT (Abcam, ab32020), VDAC (Proteintech, 55259-1-AP), β -Actin (Beyotime, AF0003), HA-tag (Abcam, ab18181), His-tag (Proteintech, 66005-1-Ig), Rabbit IgG (Bioss Antidodies, bs-0295P), Mouse IgG (Bioss Antidodies, bs-0296P), ND1 (Santacruz, sc-20493), N-Cadherin (CST, 13116S), ZEB1 (CST, 3396T), Snail (CST, 3879T), Tubulin (Beyotime, AT819), OCT4 (CST, 2750), Nanog (Abcam, ab109250), GAPDH (CST, 2118).

Cell viability assay

Cell viability assay was performed with Cell Counting Kit-8 assay (CCK-8, HY-K0301, MedChemExpress, USA) as the protocol indicated. Briefly, cells were seeded into 96-well plates. Then different concentrations of TAT-Pep or CDDP alone or their combinations were treated for 24 h or 48 h according to the experimental design. The IC50 was calculated using MatLab software.

Mitochondrial protein extraction

Mitochondrial protein was extracted using the Qproteome Mitochondria Isolation Kit (37612, QIAGEN, Germany). Firstly, cell suspensions were collected and lysed in Lysis Buffer containing protease inhibitors. Then they were centrifuged to remove the supernatant. Secondly, the left cell mass was resuspended in the Disruption Buffer containing protease inhibitors, and centrifuged at 1000 g to retain the supernatant. Then the supernatant was centrifuged at 6000 g and the left precipitation were mitochondrial components. Thirdly, the retained mitochondrial components were resuspended in Mitochondria Purification Buffer and the suspension was put onto the surface of mixture of Mitochondria

Purification Buffer and Disruption Buffer. Then precipitation was retained and supernatant was abandoned after centrifugation. Fourthly, the precipitation was resuspended with Mitochondria Storage Buffer and the supernatant was abandoned after centrifugation, until precipitation appeared at the bottom of the centrifugal tube. Then the mitochondria proteins were used for the following experiments.

Western Blot

Briefly, cells or xenograft tumors were lysed with the RIPA lysis buffer (P0013B, Beyotime, Shanghai, China) supplemented with protease inhibitors cocktail (4693116001, Roche, Switzerland). The protein supernatants were collected and protein concentration was quantified by BCA assay kit (P0012, Beyotime, Shanghai, China). Then protein supernatants were denatured with SDS-PAGE loading buffer, and equal protein was loaded to different concentrations of SDS-PAGE gels and subsequently transferred onto PVDF membranes (ISEQ00010, Millipore, Germany). Next, the membranes were blocked with 5% skimmed milk in TBST and probed with the following primary antibodies overnight at 4 °C and incubating with corresponding secondary antibodies at room temperature for 1h. Finally, the blots were visualized using an fluorescence scanner.

Co-immunoprecipitation (Co-IP)

Co-IP was performed with the Active Motif Universal Magnetic Co-IP Kit (54002, Active Motif, USA). Briefly, cells or xenograft tumors were harvested and lysed with the lysis buffer, then the supernatant was reserved after centrifugation and protein concentration was measured. Next, 2 µg indicated antibodies were added into 1000 µg protein supernatants and incubated for 2 h at 4 °C. For in vitro Co-IP, the Pep was added into the cell lysis 2 h before the antibodies. Then 25 µL magnetic beads were added into the mixture. Following overnight incubation with rotation at 4 °C, the beads were collected by magnetic shelf. Beads were resuspended and washed with 500 µL washing buffer for 3 times. Finally, the beads-enriched proteins or the whole-cell lysates (WCL) were denatured and subjected to Western Blot.

Mass spectrometry

Briefly, 293T cells overexpressing ^{DN}hTERT were lysed using SDT lysis buffer (4% SDS, 100mM Tris/HCl, 1mM DTT, pH 7.6). The hTERT antibody or control IgG was added to protein supernatants for 2 h, then protein A/G sepharose beads (sc-2003, Santa Cruz, USA) were added. After incubation overnight, the agarose was washed using the SDT lysis buffer. Then the collected beads were denatured with the SDT lysis buffer and the supernatants were subjected to subsequent mass spectrometry for protein identification. The mass spectrometry was performed by Applied Protein Technology Corporation (Shanghai, China). Mass Spectrometry results were screened by DN group vs IgG group. The detailed information was available in Table S2.

Immunofluorescence

Immunofluorescence was performed as described before using antibodies against hTERT (Abcam, ab32020), ND1 (Santacruz, sc-20493), MitoTracker (Invitrogen, M7512), DAPI (Beyotime Biotechnology, C1005).

Oxygen Consumption Rate (OCR) assays

The OCR assays were performed using the Seahorse XF extracellular flux analyzer (XFe96) (Agilent Technologies, Santa Clara, USA) with the Seahorse XF Cell Mito Stress Test Kit (103708-100, Seahorse) and Seahorse XFe96 FluxPak Plates (102416-100, Seahorse) according to the manufacturer's instructions. Briefly, 6000-8000 cells per well were seeded into the Seahorse XFp cell culture microplate overnight or treated with TAT-Pep for another 24 h. The probe plate was hydrated with deionized water for at least 4 h and then changed to calibration solution for another 1 h at 37 °C in a cell incubator without CO₂ before the assays run. The base medium (pH=7.4) was supplemented with D-glucose (10 mM), Pyruvate (1 mM) and L-glutamine (2 mM) to make the detection solution. Next, cells were washed using the detection solution and incubated in a cell incubator without CO₂ before the assays run. After baseline measurements, ATP synthase inhibitor Oligomycin (1 μM), the OXPHOS uncoupling agent FCCP (0.5 or 1 μM) and Respiratory Chain inhibitor Rotenone/Antimycin A (0.5 μM/0.5 μM) were sequentially injected into each well at the indicated time points. Data was recorded and analyzed by the Seahorse XF Wave software. Maximal Respiration was calculated as the difference between the average value of time point 7,8,9 and that of time point 10,11,12.

Extracellular acidification rate (ECAR) assays

The ECAR assays were performed using the Seahorse XF extracellular flux analyzer (XFe96) (Agilent Technologies, Santa Clara, USA) with the Seahorse XF Cell Glycolysis Stress Test Kit (103710-100, Seahorse) and Seahorse XFe96 FluxPak Plates (102416-100, Seahorse) according to the manufacturer's instructions. Briefly, 6000-8000 cells per well were seeded into the Seahorse XFp cell culture microplate overnight or treated with TAT-Pep for another 24 h. The probe plate was hydrated with deionized water for at least 4 h and then changed to calibration solution for another 1 h at 37 °C in a cell incubator without CO₂ before the assays run. The base medium (pH=7.4) was supplemented with L-glutamine (2 mM) to make the detection solution. Next, cells were washed using the detection solution and incubated in a cell incubator without CO₂ before the assays run. After baseline measurements, D-glucose (10 mM), ATP synthase inhibitor Oligomycin (1 μM), the glycolysis inhibitor 2-DG (50mM) were sequentially injected into each well at the indicated time points. Data was recorded and analyzed by the Seahorse XF Wave software. Glycolytic capacity was calculated as the difference between the average value of time point 7,8,9 and that of time point 10,11,12.

Mitochondria Complex Activity Measurement

The activities of 5 mitochondrial respiratory chain complexes were measured with their corresponding kits from Nanjing Jiancheng Bioengineering Institute (Nanjing, Jiangsu, China) described as the protocols (A089-1-1, A089-2, A089-3, A089-4-1, A089-5-1). Briefly, activities of Complex I, III, V were calculated as the

sample Specific activity by (Total activity minus Non-specific activity). Activities of Complex II and IV were calculated as the sample activity. The hallmark enzymes for measuring different Complexes were rotenone-sensitive NADH-Coenzyme Q Reductase (Complex I), sodium malonate-sensitive Succinate-Coenzyme Q Reductase (Complex II), Antimycin-sensitive Coenzyme Q-Cytochrome C Oxidoreductase (Complex III), Cytochrome C Oxidoreductase (Complex IV) and Oligomycin-sensitive ATP-synthase (Complex V).

NAD⁺ and NADH Level assays

The levels of NAD⁺ and NADH were measured according to the NAD⁺/NADH Assay Kit (Abcam, ab65348). Briefly, cells or tumors were harvested and extracted with 400uL extraction buffer following two freeze/thaw cycles. After that, the mixture was vortexed and centrifuged to collect the supernatant. To remove enzymes that may consume NADH, supernatant was filtered with the 10 kD spin column (UFC501096, Millipore, Germany) before performing the assay. To measure NADH levels, NAD⁺ was decomposed before the reaction while NADH was intact. To measure the total NAD levels, the samples were mixed with the Reaction Mix consisting of NAD Cycling Buffer and Enzyme Mix and incubated at room temperature for 5 min to cover NAD⁺ to NADH. After that, the NADH developer was added into wells and the OD 450 nm readings were taken during reaction cycled within 1-4 h. The NAD⁺ levels was calculated as the difference between total NAD levels and NADH levels.

Glucose Assay

The levels of Glucose concentration was measured using the Glucose Colorimetric/Fluorometric Assay Kit (BioVision, K606-100). Briefly, the cell culture medium was collected and the Sample Mix was prepared using the Glucose Assay Buffer (1x). Then the Glucose Reaction Mix was prepared using Glucose Assay Buffer, Glucose Probe and Glucose Enzyme Mix. After incubating the Sample Mix with Glucose Reaction Mix for 30 min protected form light at 37 °C , the absorbance at OD 570 nm was measured using the microplate reader and then the Glucose concentration was calculated.

L-Lactate Assay

The levels of Lactate concentration was measured using the L-Lactate Assay Kit II (Eton Bioscience, 200051002). Briefly, the cell culture medium was collected and the Sample Mix was prepared using the L-Lactate Assay Buffer (1x). Then the Reaction Solution was prepared using L-Lactate Assay Buffer, L-Lactate Assay Enzyme Mix and Assay Probe. After incubating the Sample Mix with the Reaction Solution for 30 min at 37 °C , the absorbance at OD 570 nm was measured using the microplate reader and then the L-Lactate concentration was calculated.

ROS generation

ROS was measured using the MitoSOX™ Red mitochondrial superoxide indicator (Thermo Fisher, M36008) as the protocol indicated. Briefly, prepare 5 mM MitoSOX™ reagent working solution. Then collect cells by digestion and centrifugation. Next, mix cells with 0.5 mL MitoSOX™ reagent working

solution (lower than 5 μM) sufficiently and incubate cells for 20 min in cell incubator. After that, wash cells gently 3 times with PBS and then perform flow cytometry to measure ROS levels.

ATP production

ATP was measured using the Kit (Beyotime Biotechnology, S0027) as the protocol indicated. Briefly, cells in 6-well plates were harvested with 200 μL lysis buffer per well, followed by centrifugation at 12000 g in 4 $^{\circ}\text{C}$ for 5 min. The supernatant was retained and protein concentration was measured for subsequent detection. Besides, ATP detection reagent was diluted using the dilution reagent with volume ratio of 1:4, which resulted in the working solution. Transfer 100 μL of the working solution into the detection hole, and placed for 3 to 5 min at room temperature. Add 20 μL protein supernatant into the detection hole, and mix rapidly with pipettor. After at least 2 sec, the RLU value was measured by the chemiluminescence instrument, and the ATP level was reflected by the ratio of RLU value to protein concentration.

TRAP experiments

The telomeric repeat amplification protocol (TRAP) experiment was performed using the Telomerase activity detection kit (Millipore, S7700) as described.

PDX models establishment and experiments

The PDX models were built with 6-8-week-old male immunocompromised NOD-SCID IL2R γ ^{-/-} (B-NDG) mouse (Biocytogen, Beijing, China). Briefly, all HCC specimens were directly got from surgical operating room and transported in fresh cell culture medium containing 20% penicillin/streptomycin on ice. Specimens were washed with cold fresh culture medium, then necrotic tissues, adipose tissues and fibrous tissues were removed carefully, and the retained authentic tumor tissues (about 30-50 mm³) were used for transplantation. After that, the B-NDG mouse was narcotized. The tumor mass was cut into small pieces and then mixed adequately with Matrigel (356234, Corning, USA,). Then the small pieces were stuffed into the needle tubing and implanted subcutaneously into two sides of the humeral back via a skin incision over the lumbar spine. Finally, the incision was covered with antibiotic dry powder. The whole process was performed in sterile animal operating table. The successful transplantation with visible new tumors was named Generation F0. When the tumor volume reached about 1 cm³, Generation F0 was transplanted into more B-NDG mice for quantity amplification as the above process. The resultant usable tumor-bearing B-NDG mice were named Generation F1. After transplantation to the Generation F3 with sufficient mice quantity with comparable tumor volumes, the mice were randomly divided into the corresponding groups (5 mice each group with the approximative average tumor volumes). Generation F3 of Sample 29 was treated with vehicle control or TAT-Pep (tail intravenous injection, 500 $\mu\text{g}/\text{kg}$). Generation F3 of Sample 35 was treated with vehicle control, TAT-Pep (tail intravenous injection, 500 $\mu\text{g}/\text{kg}$), CDDP (intraperitoneal injection, 3 mg/kg) or the combination of TAT-Pep with CDDP. TAT-Pep and CDDP were dissolved in PBS. TAT-Pep was treated every day and CDDP was treated once every 3 days. Tumor volume was measured with electric calipers, and tumor volume (cm³) = long diameter \times (short diameter)²/2. After treatments for 18 days, the PDX tumors were harvested and used for the subsequent

experiments. The residual tumor tissues from Generation F0 to F3 were cut into small fragments and preserved in 4% paraformaldehyde or liquid nitrogen, respectively. All animal experiments were approved by the Animal Care and Use Committee of Third Military Medical University.

Peptide

The sequence for peptide (Pep) and the cell-penetrating peptide (TAT-Pep) was GPFALFFMAEYT and YGRKKRRQRRRGPFALFFMAEYT, respectively. The TAT-Pep-Luc was designed as YGRKKRRQRRRGPFALFFMAEYT[Lys(FITC)], with a Lys(FITC) group at the C end of TAT-Pep. They were all synthesized by Genescript Cooperation (Nanjing, China).

Statistical analyses

GraphPad Prism 9.0 was used for statistical analysis. All data were expressed as mean \pm SD unless otherwise stated. Comparisons between two groups normally distributed were determined using the unpaired Student's test (t test). Non-normally distributed variables between two groups were compared using the Mann-Whitney U test. Statistical methods for TCGA data were described in Legend of Supplementary Figure S1. * means $P < 0.05$, ** means $P < 0.01$, *** means $P < 0.001$, NS means not significant. $P < 0.05$ was considered statistically significant.

References

1. Asghar, U. & Meyer, T. Are there opportunities for chemotherapy in the treatment of hepatocellular cancer? *J Hepatol* 56, 686-695, doi:10.1016/j.jhep.2011.07.031 (2012).
2. Cook, A. M., Lesterhuis, W. J., Nowak, A. K. & Lake, R. A. Chemotherapy and immunotherapy: mapping the road ahead. *Curr Opin Immunol* 39, 23-29, doi:10.1016/j.coi.2015.12.003 (2016).
3. Serkova, N. J. & Eckhardt, S. G. Metabolic Imaging to Assess Treatment Response to Cytotoxic and Cytostatic Agents. *Front Oncol* 6, 152, doi:10.3389/fonc.2016.00152 (2016).
4. Rottenberg, S., Disler, C. & Perego, P. The rediscovery of platinum-based cancer therapy. *Nat Rev Cancer* 21, 37-50, doi:10.1038/s41568-020-00308-y (2021).
5. Mosca, L., Ilari, A., Fazi, F., Assaraf, Y. G. & Colotti, G. Taxanes in cancer treatment: Activity, chemoresistance and its overcoming. *Drug Resist Updat* 54, 100742, doi:10.1016/j.drug.2020.100742 (2021).
6. Holohan, C., Van Schaeybroeck, S., Longley, D. B. & Johnston, P. G. Cancer drug resistance: an evolving paradigm. *Nat Rev Cancer* 13, 714-726, doi:10.1038/nrc3599 (2013).
7. Bukowski, K., Kciuk, M. & Kontek, R. Mechanisms of Multidrug Resistance in Cancer Chemotherapy. *Int J Mol Sci* 21, doi:10.3390/ijms21093233 (2020).
8. Assaraf, Y. G. et al. The multi-factorial nature of clinical multidrug resistance in cancer. *Drug Resist Updat* 46, 100645, doi:10.1016/j.drug.2019.100645 (2019).

9. DeBerardinis, R. J., Lum, J. J., Hatzivassiliou, G. & Thompson, C. B. The Biology of Cancer: Metabolic Reprogramming Fuels Cell Growth and Proliferation. *Cell Metabolism* 7, 11-20, doi:10.1016/j.cmet.2007.10.002 (2008).
10. Ward, P. S. & Thompson, C. B. Metabolic reprogramming: a cancer hallmark even warburg did not anticipate. *Cancer Cell* 21, 297-308, doi:10.1016/j.ccr.2012.02.014 (2012).
11. Vander Heiden, M. G., Cantley, L. C. & Thompson, C. B. Understanding the Warburg effect: the metabolic requirements of cell proliferation. *Science* 324, 1029-1033, doi:10.1126/science.1160809 (2009).
12. Icard, P. et al. How the Warburg effect supports aggressiveness and drug resistance of cancer cells? *Drug Resist Updat* 38, 1-11, doi:10.1016/j.drug.2018.03.001 (2018).
13. Serna-Blasco, R., Sanz-Alvarez, M., Aguilera, O. & Garcia-Foncillas, J. Targeting the RAS-dependent chemoresistance: The Warburg connection. *Semin Cancer Biol* 54, 80-90, doi:10.1016/j.semcancer.2018.01.016 (2019).
14. Bhattacharya, B., Mohd Omar, M. F. & Soong, R. The Warburg effect and drug resistance. *Br J Pharmacol* 173, 970-979, doi:10.1111/bph.13422 (2016).
15. Ghareghomi, S., Ahmadian, S., Zarghami, N. & Kahroba, H. Fundamental insights into the interaction between telomerase/TERT and intracellular signaling pathways. *Biochimie* 181, 12-24, doi:10.1016/j.biochi.2020.11.015 (2021).
16. Mocellin, S., Pooley, K. A. & Nitti, D. Telomerase and the search for the end of cancer. *Trends Mol Med* 19, 125-133, doi:10.1016/j.molmed.2012.11.006 (2013).
17. Low, K. C. & Tergaonkar, V. Telomerase: central regulator of all of the hallmarks of cancer. *Trends Biochem Sci* 38, 426-434, doi:10.1016/j.tibs.2013.07.001 (2013).
18. Maciejowski, J. & de Lange, T. Telomeres in cancer: tumour suppression and genome instability. *Nat Rev Mol Cell Biol* 18, 175-186, doi:10.1038/nrm.2016.171 (2017).
19. Zhang, P., Chan, S. L., Fu, W., Mendoza, M. & Mattson, M. P. TERT suppresses apoptosis at a premitochondrial step by a mechanism requiring reverse transcriptase activity and 14-3-3 protein-binding ability. *FASEB J* 17, 767-769, doi:10.1096/fj.02-0603fje (2003).
20. Rosen, J., Jakobs, P., Ale-Agha, N., Altschmied, J. & Haendeler, J. Non-canonical functions of Telomerase Reverse Transcriptase - Impact on redox homeostasis. *Redox Biol* 34, 101543, doi:10.1016/j.redox.2020.101543 (2020).
21. Indran, I. R., Hande, M. P. & Pervaiz, S. Tumor cell redox state and mitochondria at the center of the non-canonical activity of telomerase reverse transcriptase. *Mol Aspects Med* 31, 21-28, doi:10.1016/j.mam.2009.12.001 (2010).
22. Hu, C. et al. hTERT promotes the invasion of gastric cancer cells by enhancing FOXO3a ubiquitination and subsequent ITGB1 upregulation. *Gut* 66, 31-42, doi:10.1136/gutjnl-2015-309322 (2017).
23. Santos, J. H., Meyer, J. N., Skorvaga, M., Annab, L. A. & Van Houten, B. Mitochondrial hTERT exacerbates free-radical-mediated mtDNA damage. *Aging Cell* 3, 399-411, doi:10.1111/j.1474-

9728.2004.00124.x (2004).

24. Indran, I. R., Hande, M. P. & Pervaiz, S. hTERT overexpression alleviates intracellular ROS production, improves mitochondrial function, and inhibits ROS-mediated apoptosis in cancer cells. *Cancer Res* 71, 266-276, doi:10.1158/0008-5472.CAN-10-1588 (2011).
25. Haendeler, J. et al. Mitochondrial telomerase reverse transcriptase binds to and protects mitochondrial DNA and function from damage. *Arterioscler Thromb Vasc Biol* 29, 929-935, doi:10.1161/ATVBAHA.109.185546 (2009).
26. Ahmed, S. et al. Telomerase does not counteract telomere shortening but protects mitochondrial function under oxidative stress. *J Cell Sci* 121, 1046-1053, doi:10.1242/jcs.019372 (2008).
27. Martens, A., Schmid, B., Akintola, O. & Saretzki, G. Telomerase Does Not Improve DNA Repair in Mitochondria upon Stress but Increases MnSOD Protein under Serum-Free Conditions. *Int J Mol Sci* 21, doi:10.3390/ijms21010027 (2019).
28. Sharma, N. K. et al. Human telomerase acts as a hTR-independent reverse transcriptase in mitochondria. *Nucleic Acids Res* 40, 712-725, doi:10.1093/nar/gkr758 (2012).
29. Santos, J. H., Meyer, J. N. & Van Houten, B. Mitochondrial localization of telomerase as a determinant for hydrogen peroxide-induced mitochondrial DNA damage and apoptosis. *Hum Mol Genet* 15, 1757-1768, doi:10.1093/hmg/ddl098 (2006).
30. Yan, J. et al. Effects of mitochondrial translocation of telomerase on drug resistance in hepatocellular carcinoma cells. *J Cancer* 6, 151-159, doi:10.7150/jca.10419 (2015).
31. Ling, X., Wen, L. & Zhou, Y. Role of mitochondrial translocation of telomerase in hepatocellular carcinoma cells with multidrug resistance. *Int J Med Sci* 9, 545-554, doi:10.7150/ijms.4648 (2012).
32. Zhang, Z. et al. Telomerase reverse transcriptase promotes chemoresistance by suppressing cisplatin-dependent apoptosis in osteosarcoma cells. *Sci Rep* 7, 7070, doi:10.1038/s41598-017-07204-w (2017).
33. Singhapol, C. et al. Mitochondrial telomerase protects cancer cells from nuclear DNA damage and apoptosis. *PLoS One* 8, e52989, doi:10.1371/journal.pone.0052989 (2013).
34. Guerra, F., Arbin, A. A. & Moro, L. Mitochondria and cancer chemoresistance. *Biochim Biophys Acta Bioenerg* 1858, 686-699, doi:10.1016/j.bbabi.2017.01.012 (2017).
35. Karamanlidis, G. et al. Mitochondrial complex I deficiency increases protein acetylation and accelerates heart failure. *Cell Metab* 18, 239-250, doi:10.1016/j.cmet.2013.07.002 (2013).
36. Stefanatos, R. & Sanz, A. Mitochondrial complex I: a central regulator of the aging process. *Cell Cycle* 10, 1528-1532, doi:10.4161/cc.10.10.15496 (2011).
37. Santidrian, A. F. et al. Mitochondrial complex I activity and NAD⁺/NADH balance regulate breast cancer progression. *J Clin Invest* 123, 1068-1081, doi:10.1172/JCI64264 (2013).
38. Sharma, L. K. et al. Mitochondrial respiratory complex I dysfunction promotes tumorigenesis through ROS alteration and AKT activation. *Hum Mol Genet* 20, 4605-4616, doi:10.1093/hmg/ddr395 (2011).

39. Hirst, J. Mitochondrial complex I. *Annu Rev Biochem* 82, 551-575, doi:10.1146/annurev-biochem-070511-103700 (2013).
40. Viswanath, P. et al. Metabolic imaging detects elevated glucose flux through the pentose phosphate pathway associated with TERT expression in low-grade gliomas. *Neuro Oncol* 23, 1509-1522, doi:10.1093/neuonc/noab093 (2021).
41. Ahmad, F. et al. Telomerase reverse transcriptase (TERT) - enhancer of zeste homolog 2 (EZH2) network regulates lipid metabolism and DNA damage responses in glioblastoma. *J Neurochem* 143, 671-683, doi:10.1111/jnc.14152 (2017).
42. Urra, F. A., Munoz, F., Lovy, A. & Cardenas, C. The Mitochondrial Complex(I)ty of Cancer. *Front Oncol* 7, 118, doi:10.3389/fonc.2017.00118 (2017).
43. Leone, G., Abla, H., Gasparre, G., Porcelli, A. M. & Iommarini, L. The Oncojanus Paradigm of Respiratory Complex I. *Genes (Basel)* 9, doi:10.3390/genes9050243 (2018).
44. Sahin, E. et al. Telomere dysfunction induces metabolic and mitochondrial compromise. *Nature* 470, 359-365, doi:10.1038/nature09787 (2011).
45. Sherman, J., Verstandig, G. & Brumer, Y. Application of machine learning to large in-vitro databases to identify cancer cell characteristics: telomerase reverse transcriptase (TERT) expression. *Oncogene* 40, 5038-5041, doi:10.1038/s41388-021-01894-3 (2021).
46. Ale-Agha, N. et al. Mitochondrial Telomerase Reverse Transcriptase Protects From Myocardial Ischemia/Reperfusion Injury by Improving Complex I Composition and Function. *Circulation* 144, 1876-1890, doi:10.1161/CIRCULATIONAHA.120.051923 (2021).
47. Iommarini, L. et al. Different mtDNA mutations modify tumor progression in dependence of the degree of respiratory complex I impairment. *Hum Mol Genet* 23, 1453-1466, doi:10.1093/hmg/ddt533 (2014).
48. Vercellino, I. & Sazanov, L. A. The assembly, regulation and function of the mitochondrial respiratory chain. *Nat Rev Mol Cell Biol* 23, 141-161, doi:10.1038/s41580-021-00415-0 (2022).
49. Zhu, J., Vinothkumar, K. R. & Hirst, J. Structure of mammalian respiratory complex I. *Nature* 536, 354-358, doi:10.1038/nature19095 (2016).
50. Sanchez-Caballero, L., Guerrero-Castillo, S. & Nijtmans, L. Unraveling the complexity of mitochondrial complex I assembly: A dynamic process. *Biochim Biophys Acta* 1857, 980-990, doi:10.1016/j.bbabi.2016.03.031 (2016).
51. Pinheiro, M. et al. Mitochondrial genome alterations in rectal and sigmoid carcinomas. *Cancer Lett* 280, 38-43, doi:10.1016/j.canlet.2009.02.009 (2009).
52. Guleng, G., Lovig, T., Meling, G. I., Andersen, S. N. & Rognum, T. O. Mitochondrial microsatellite instability in colorectal carcinomas—frequency and association with nuclear microsatellite instability. *Cancer Lett* 219, 97-103, doi:10.1016/j.canlet.2004.07.018 (2005).
53. Xu, Y. et al. Quantitative detection of circulating MT-ND1 as a potential biomarker for colorectal cancer. *Bosn J Basic Med Sci* 21, 577-586, doi:10.17305/bjbms.2021.5576 (2021).

54. Parrella, P. et al. Detection of mitochondrial DNA mutations in primary breast cancer and fine-needle aspirates. *Cancer Res* 61, 7623-7626 (2001).
55. Kim, H. et al. Mutations in the Mitochondrial ND1 Gene Are Associated with Postoperative Prognosis of Localized Renal Cell Carcinoma. *Int J Mol Sci* 17, doi:10.3390/ijms17122049 (2016).
56. Dmitrenko, V. et al. Reduction of the transcription level of the mitochondrial genome in human glioblastoma. *Cancer Lett* 218, 99-107, doi:10.1016/j.canlet.2004.07.001 (2005).
57. Jiang, Z. et al. Diagnostic value of circulating cell-free mtDNA in patients with suspected thyroid cancer: ND4/ND1 ratio as a new potential plasma marker. *Mitochondrion* 55, 145-153, doi:10.1016/j.mito.2020.09.007 (2020).
58. Gasparre, G. et al. A mutation threshold distinguishes the antitumorigenic effects of the mitochondrial gene MTND1, an oncojanus function. *Cancer Res* 71, 6220-6229, doi:10.1158/0008-5472.CAN-11-1042 (2011).
59. Calabrese, C. et al. Respiratory complex I is essential to induce a Warburg profile in mitochondria-defective tumor cells. *Cancer Metab* 1, 11, doi:10.1186/2049-3002-1-11 (2013).
60. Bonora, E. et al. Defective oxidative phosphorylation in thyroid oncocyctic carcinoma is associated with pathogenic mitochondrial DNA mutations affecting complexes I and III. *Cancer Res* 66, 6087-6096, doi:10.1158/0008-5472.CAN-06-0171 (2006).
61. Mayr, J. A. et al. Loss of complex I due to mitochondrial DNA mutations in renal oncocytoma. *Clin Cancer Res* 14, 2270-2275, doi:10.1158/1078-0432.CCR-07-4131 (2008).
62. Gutierrez Cortes, N. et al. Mutation m.3395A > G in MT-ND1 leads to variable pathologic manifestations. *Hum Mol Genet* 29, 980-989, doi:10.1093/hmg/ddaa020 (2020).
63. Zurita Rendon, O. & Shoubridge, E. A. Early complex I assembly defects result in rapid turnover of the ND1 subunit. *Hum Mol Genet* 21, 3815-3824, doi:10.1093/hmg/dds209 (2012).
64. Zurita Rendon, O., Silva Neiva, L., Sasarman, F. & Shoubridge, E. A. The arginine methyltransferase NDUFAF7 is essential for complex I assembly and early vertebrate embryogenesis. *Hum Mol Genet* 23, 5159-5170, doi:10.1093/hmg/ddu239 (2014).
65. Rhein, V. F., Carroll, J., Ding, S., Fearnley, I. M. & Walker, J. E. NDUFAF5 Hydroxylates NDUFS7 at an Early Stage in the Assembly of Human Complex I. *J Biol Chem* 291, 14851-14860, doi:10.1074/jbc.M116.734970 (2016).
66. Ugalde, C. et al. Human mitochondrial complex I assembles through the combination of evolutionary conserved modules: a framework to interpret complex I deficiencies. *Hum Mol Genet* 13, 2461-2472, doi:10.1093/hmg/ddh262 (2004).
67. Lim, S. C. et al. Loss of mitochondrial DNA-encoded protein ND1 results in disruption of complex I biogenesis during early stages of assembly. *FASEB J* 30, 2236-2248, doi:10.1096/fj.201500137R (2016).

Declarations

COMPETING INTERESTS

All authors declare that there are no competing interests.

ADDITIONAL INFORMATION

Supplemental information can be found online.

Figures

Figure 1

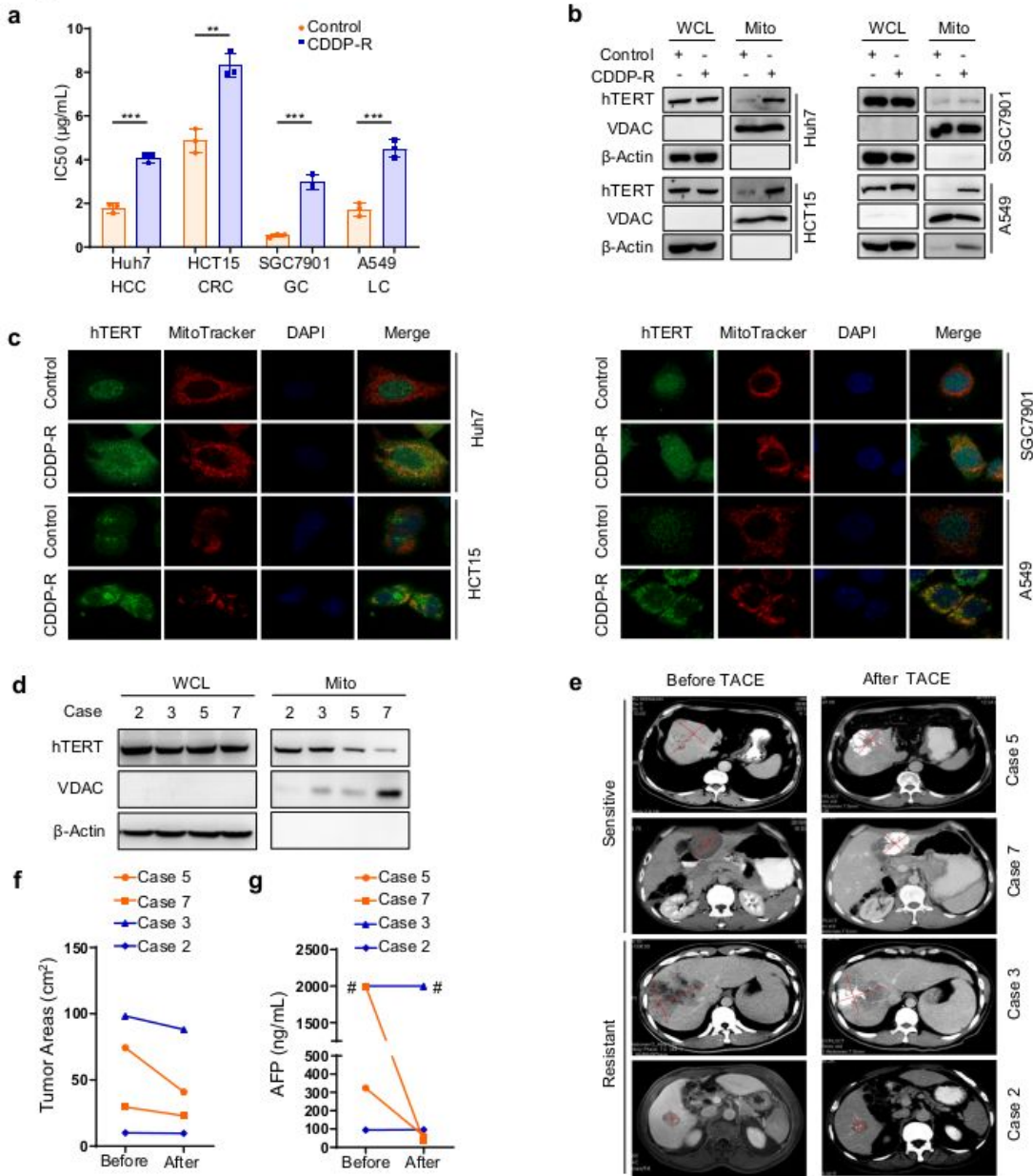


Figure 1

Mitochondrial hTERT negatively influences cancer response to chemotherapy

(A) Huh7 (HCC) CDDP-R, HCT15 (colorectal cancer, CRC) CDDP-R, SGC7901 (gastric cancer, GC) CDDP-R, A549 (lung cancer, LC) CDDP-R and their corresponding control parental cells were treated with different concentrations of CDDP for 48h, then the IC50 levels were calculated. **(B)** The whole cell lysates (WCL)

and mitochondrial components in Huh7 CDDP-R, HCT15 CDDP-R, SGC7901 CDDP-R, A549 CDDP-R cells and their corresponding control parental cells were extracted respectively. Then hTERT was detected by Western Blot, taking β -Actin and VDAC as the WCL and mitochondrial loading controls, respectively. **(C)** Immunofluorescence detection of mitochondrial hTERT in Huh7 CDDP-R, HCT15 CDDP-R, SGC7901 CDDP-R, A549 CDDP-R and their corresponding control parental cells. Mitochondria was stained with MitoTracker and cell nucleus was stained with DAPI. **(D)** The WCL and mitochondrial proteins of tumor specimens before TACE from 4 HCC patients were extracted. Then hTERT was detected by Western Blot, taking β -Actin and VDAC as the WCL and mitochondrial loading controls, respectively. **(E)** CT or MRI images of representative HCC cases before and after TACE were shown. **(F)** Tumor areas in the above images were calculated and shown. **(G)** AFP levels before and after TACE were shown. # means AFP level was higher than 2000 ng/mL. ***, $P < 0.001$; **, $P < 0.01$.

Figure 2

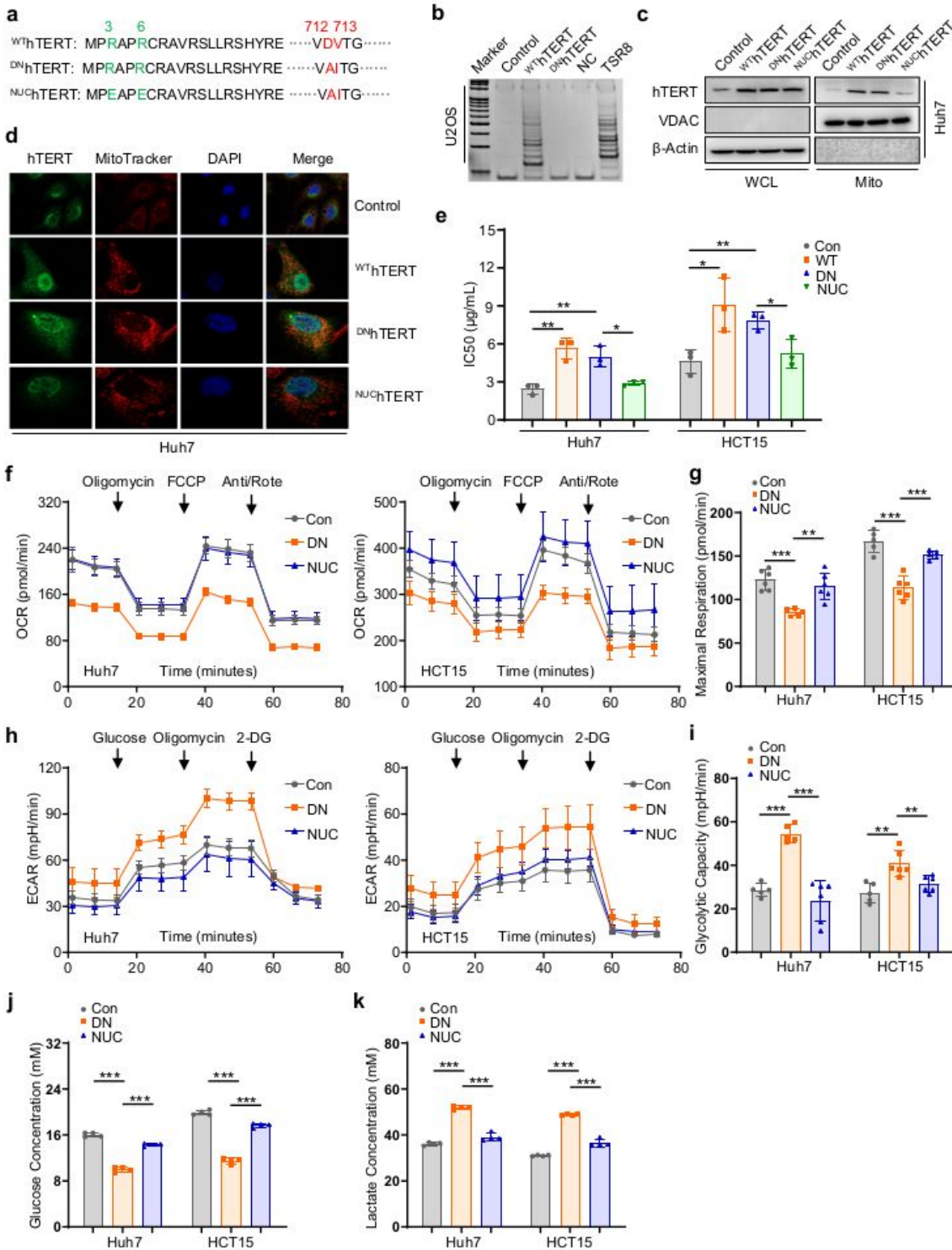


Figure 2

Mitochondrial hTERT rewire cellular glucose metabolism and confers chemoresistance in a telomerase RT independent manner

(A) The key amino acids that determines the telomerase RT activity of hTERT and corresponding mutants were shown in red color. The key amino acids that determine the mitochondrial location of hTERT and

corresponding mutants were shown in green color. **(B)** U2OS cells were stably transfected with ^{WT}hTERT, ^{DN}hTERT or Control lentiviruses, then the telomerase RT activity were detected by TRAP assays in the indicated treatments. Taking NC as negative control and TSR8 as positive control. **(C)** Huh7 cells were stably transfected with ^{WT}hTERT, ^{DN}hTERT, ^{NUC}hTERT or Control lentiviruses, then hTERT was detected by Western Blot. β -Actin and VDAC were taken as the WCL and mitochondrial loading controls, respectively. **(D)** Immunofluorescence detection of mitochondrial hTERT in Huh7 ^{WT}hTERT, ^{DN}hTERT, ^{NUC}hTERT and Control cells. Mitochondria was stained with MitoTracker and cell nucleus was stained with DAPI. **(E)** Huh7 or HCT15 ^{WT}hTERT, ^{DN}hTERT, ^{NUC}hTERT and Control cells were treated with different concentrations of CDDP for 48h, then the IC50 levels were calculated. **(F)** The OCRs of Huh7 or HCT15 ^{DN}hTERT, ^{NUC}hTERT and Control cells were evaluated by the Seahorse XFe96 extracellular flux analyzer, with the treatment of Oligomycin, FCCP and Antimycin/Rotenone at the indicated times. **(G)** The maximal respiration levels of OCRs in (F) were calculated. **(H)** The ECARs of Huh7 or HCT15 ^{DN}hTERT, ^{NUC}hTERT and Control cells were evaluated by the Seahorse XFe96 extracellular flux analyzer, with the treatment of Glucose, Oligomycin and 2-DG at the indicated times. **(I)** The glycolytic capacity levels of ECARs in (H) were calculated. **(J-K)** The glucose or L-lactate levels of Huh7 or HCT15 ^{DN}hTERT, ^{NUC}hTERT and Control cells were measured. *******, $P < 0.001$; ******, $P < 0.01$; *****, $P < 0.05$.

Figure 3

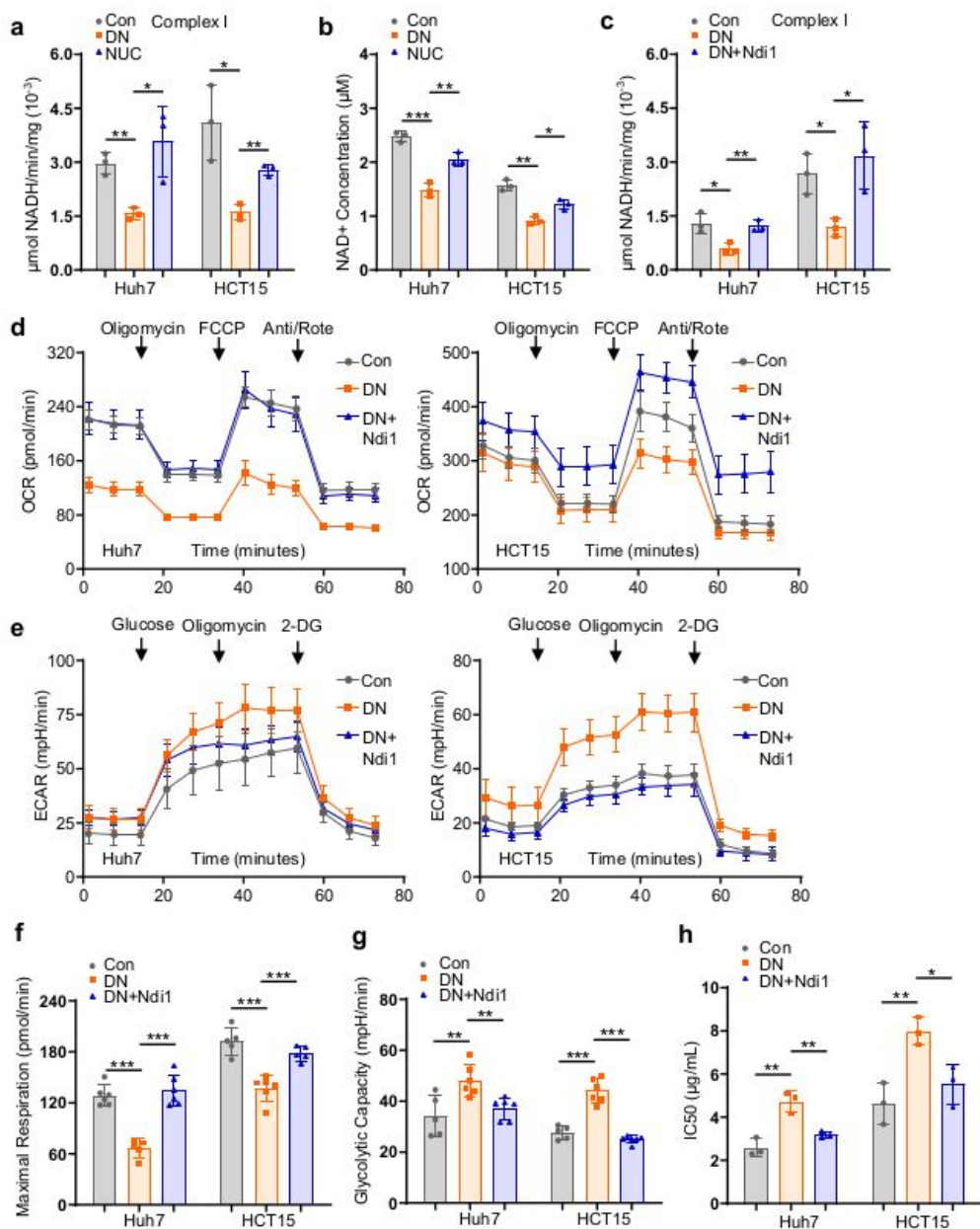


Figure 3

hTERT reprograms mitochondrial metabolism via inhibiting Complex I activity

(A) Mitochondria Complex I activities of Huh7 or HCT15 ^{DN}hTERT, ^{NUC}hTERT and Control cells were measured. **(B)** The NAD⁺ levels of Huh7 or HCT15 ^{DN}hTERT, ^{NUC}hTERT and Control cells were measured. **(C)** Mitochondria Complex I activities of Huh7 or HCT15 ^{DN}hTERT, ^{DN}hTERT+Ndi1 and Control cells were

measured. **(D)** The OCRs of Huh7 or HCT15 ^{DN}hTERT, ^{DN}hTERT+Ndi1 and Control cells were evaluated by the Seahorse XFe96 extracellular flux analyzer, with the treatment of Oligomycin, FCCP and Antimycin/Rotenone at the indicated times. **(E)** The ECARs of Huh7 or HCT15 ^{DN}hTERT, ^{DN}hTERT+Ndi1 and Control cells were evaluated by the Seahorse XFe96 extracellular flux analyzer, with the treatment of Glucose, Oligomycin and 2-DG at the indicated times. **(F)** The maximal respiration levels of OCRs in (D) were calculated. **(G)** The glycolytic capacity levels of ECARs in (E) were calculated. **(H)** Huh7 or HCT15 ^{DN}hTERT, ^{DN}hTERT+Ndi1 and Control cells were treated with different concentrations of CDDP for 48h, then the IC50 levels were calculated. ***, $P < 0.001$; **, $P < 0.01$; *, $P < 0.05$.

Figure 4

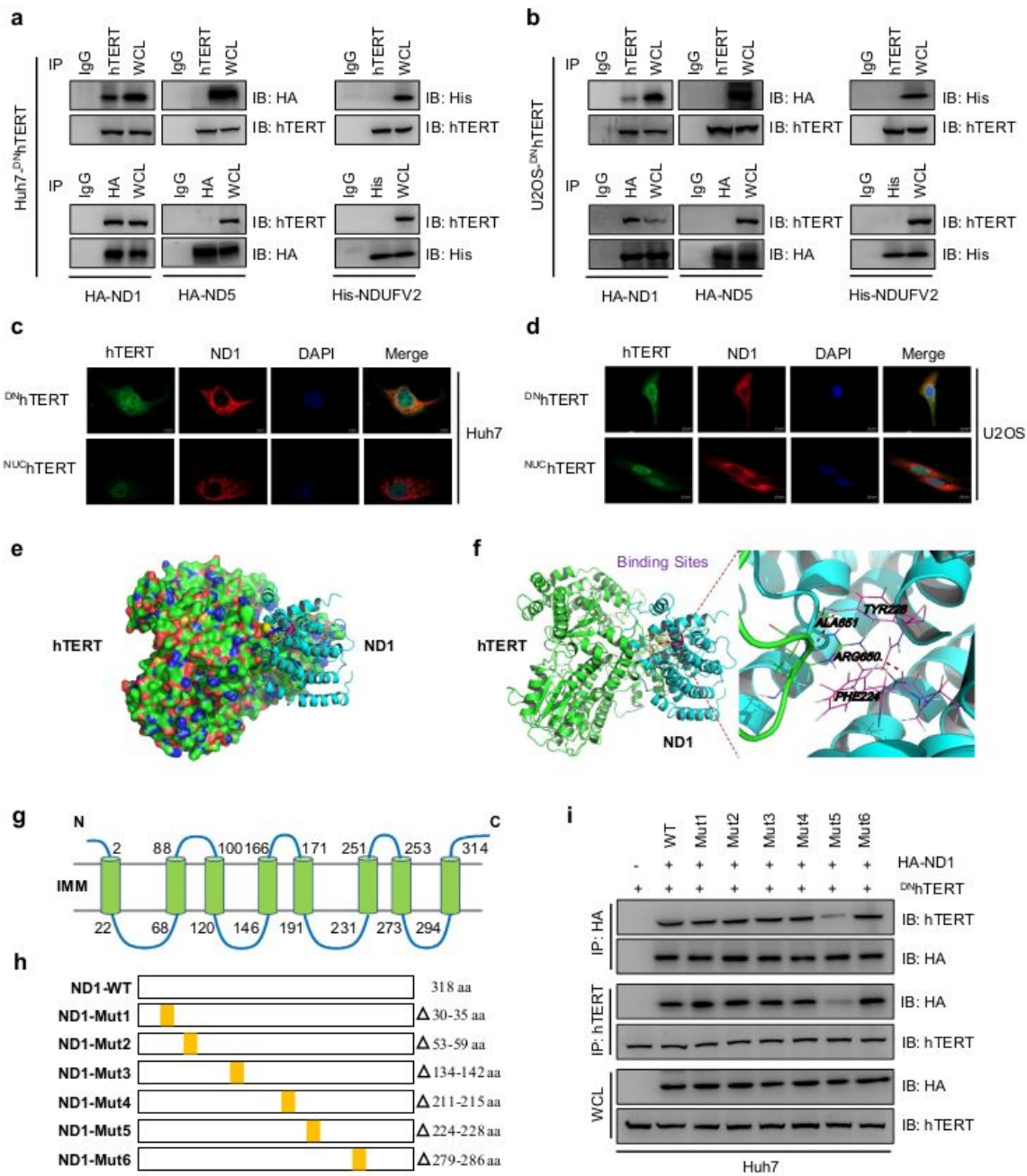


Figure 4

Mitochondrial hTERT physically interacts with the Complex I subunit MT-ND1

(A-B) After transfection with HA-ND1 or HA-ND5 (or His-NDUFV2) in Huh7^{DNhTERT} cells or U2OS^{DNhTERT} cells respectively, cell lysates were harvested and then immunoprecipitated with hTERT antibody and control IgG or HA (or His) antibody and control IgG, then HA (or His) and hTERT were

detected by Western Blot using the corresponding precipitates or WCL. **(C-D)** Immunofluorescence detection of the colocalizations of mitochondrial hTERT and ND1 in Huh7 (C) or U2OS (D) ^{DN}hTERT and ^{NUC}hTERT cells. Cell nucleus was stained with DAPI. **(E-F)** Z-Dock prediction of potential interaction between hTERT and ND1. **(G)** The structure model of ND1 protein. IMM, inner mitochondrial membrane. **(H)** Schematic diagram showing wide type (WT) and variant deletion mutation regions of ND1 protein. **(I)** After transfection with WT HA-ND1, mutant1-6 (Mut1-6) HA-ND1 respectively or control vector in Huh7 ^{DN}hTERT cells, cell lysates were harvested and then immunoprecipitated with HA antibody or hTERT antibody, then hTERT and HA were detected by Western Blot using the corresponding precipitates or WCL.

Figure 5

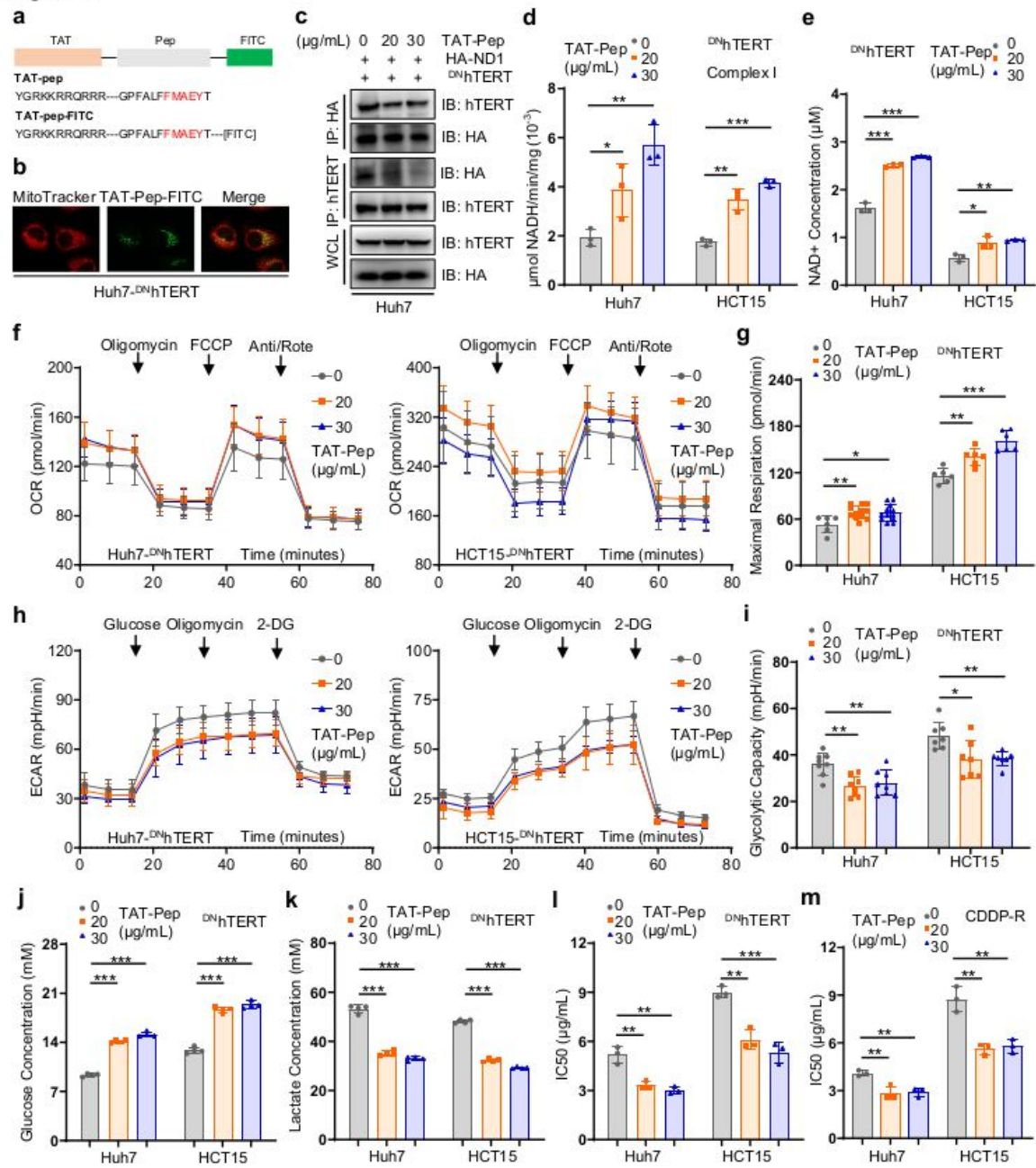


Figure 5

Blocking interaction between hTERT and ND1 by a novel TAT-Pep weakens Warburg effect and enhances chemosensitivity

(A) The model graph showing structure and amino acid sequence of TAT-Pep or TAT-Pep-FITC. **(B)** After treatment with the TAT-Pep-FITC for 24h in Huh7^{DN}hTERT cells, the localization of TAT-Pep in

mitochondria was analyzed by immunofluorescence. Mitochondria was stained with MitoTracker. **(C)** After transfection with HA-ND1, Huh7^{DN}hTERT cells were treated with different concentrations of TAT-Pep for 24h, then cell lysates were harvested and then immunoprecipitated with HA antibody or hTERT antibody, then hTERT and HA were detected by Western Blot using the corresponding precipitates or WCL. **(D)** Huh7^{DN}hTERT cells or HCT15^{DN}hTERT cells were treated with different concentrations of TAT-Pep for 24h, then the mitochondria Complex I activities were measured. **(E)** Huh7^{DN}hTERT cells or HCT15^{DN}hTERT cells were treated with different concentrations of TAT-Pep for 24h, then the NAD⁺ levels were measured. **(F)** Huh7 or HCT15^{DN}hTERT cells were treated with different concentrations of TAT-Pep for 24h, then the OCRs were evaluated by the Seahorse XFe96 extracellular flux analyze, with the treatment of Oligomycin, FCCP and Antimycin/Rotenone at the indicated times. **(G)** The maximal respiration levels of OCRs in (F) were calculated. **(H)** Huh7 or HCT15^{DN}hTERT cells were treated with different concentrations of TAT-Pep for 24h, then the ECARs were evaluated by the Seahorse XFe96p extracellular flux analyze, with the treatment of Glucose, Oligomycin and 2-DG at the indicated times. **(I)** The glycolytic capacity levels of ECARs in (H) were calculated. **(J-K)** Huh7 or HCT15^{DN}hTERT cells were treated with different concentrations of TAT-Pep for 24h, then the Glucose or L-lactate levels were measured. **(L-M)** After pretreatment with different concentrations of TAT-Pep for 24h, Huh7^{DN}hTERT cells or HCT15^{DN}hTERT cells (L), or Huh7 CDDP-R cells or HCT15 CDDP-R cells (M) were treated with the combinations of different concentrations of TAT-Pep and CDDP for 48h, then the IC₅₀ levels were calculated. ***, $P < 0.001$; **, $P < 0.01$; * $P < 0.05$.

Figure 6

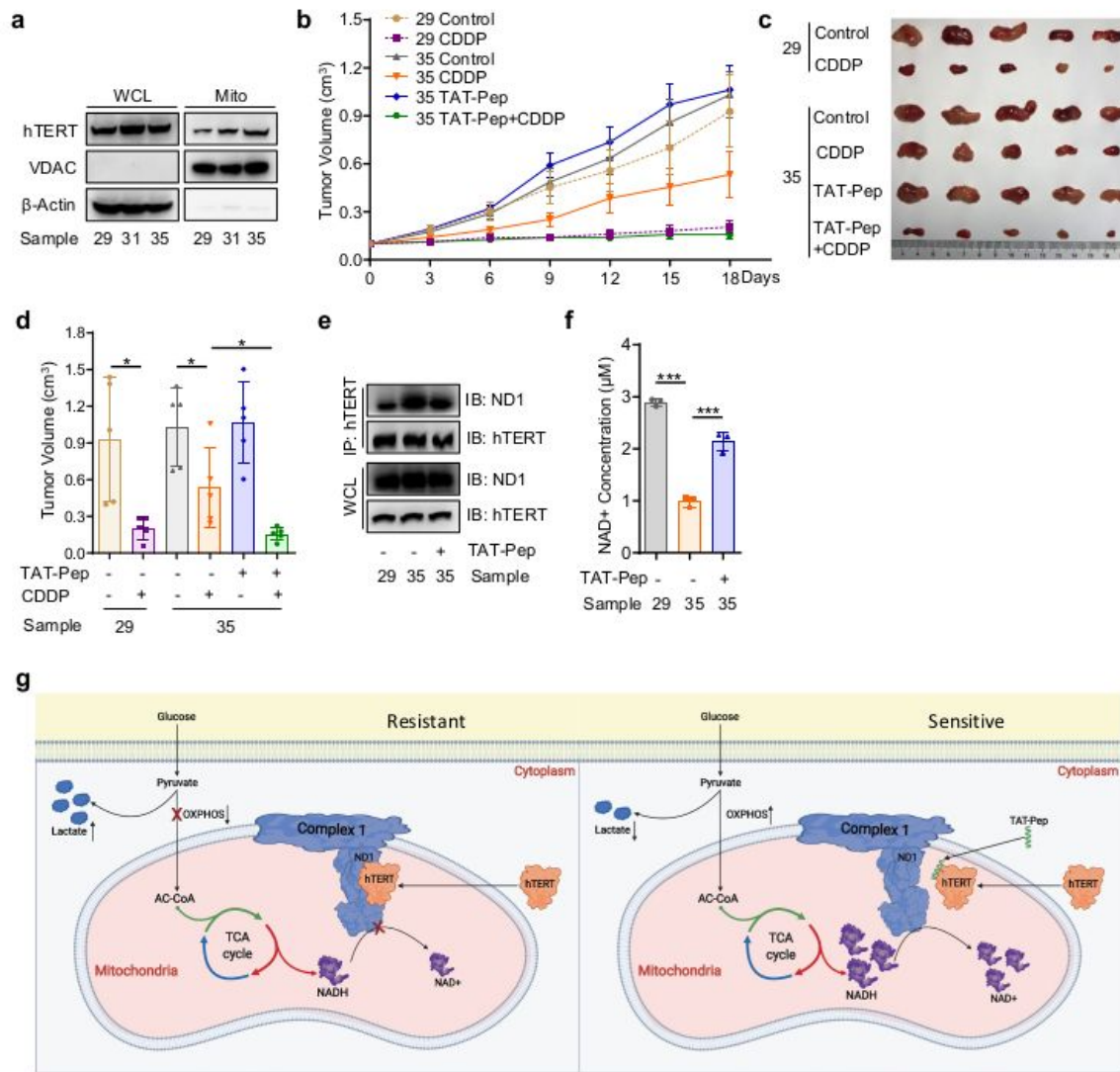


Figure 6

Disrupting the hTERT/ND1 interaction enhances therapeutic effects of CDDP in PDX tumor models

(A) The WCL and mitochondrial proteins of HCC tumor samples were extracted. Then hTERT was detected by Western Blot, taking β -Actin and VDAC as the WCL and mitochondrial loading controls, respectively. **(B)** NSG mice bearing the F₃ Generation PDX tumors were randomly grouped (n=5). Then

PDX tumors of Sample 29 were treated with vehicle control or TAT-Pep. PDX tumors of Sample 35 were treated with vehicle control, TAT-Pep, CDDP or the combination of TAT-Pep/CDDP. The continuous changes of the PDX tumor volumes were shown (Error bars represent SEM.). **(C)** After drug treatment, mice were sacrificed and the xenograft tumors were shown. **(D)** The average tumor volumes for each treatment group in (C) were calculated (Error bars represent SEM.). **(E)** Representative PDX tumors from the indicated groups were lysed and the lysates were immunoprecipitated with hTERT antibody, then ND1 and hTERT were detected by Western Blot using the corresponding precipitates or WCL. **(F)** The NAD⁺ levels of representative PDX tumors from the indicated groups were measured. **(H)** Schematic revealing the effects of hTERT/ND1 interaction or its blockage by TAT-Pep on Warburg effect and chemotherapeutic effects. The mitochondrial hTERT interacts with Complex I core subunit ND1 to disturbs Complex I assembly and inhibits its activity, which reprograms cancer metabolism towards Warburg effect (repressed OXPHOS and TCA cycle coupled with elevated ECAR, lactate production and glucose consumption) and finally leads to chemotherapy resistance (Left). Disrupting the interaction between hTERT and ND1 using the TAT-Pep recovers the Complex I activity, which reverses the Warburg effect (enhanced OXPHOS and TCA cycle coupled with weakened ECAR, lactate production and glucose consumption) and favors chemosensitivity (Right). *******, $P < 0.001$; ***** $P < 0.05$.

Supplementary Files

This is a list of supplementary files associated with this preprint. Click to download.

- [SupplementaryTableS1.xlsx](#)
- [SupplementaryTableS2.xlsx](#)
- [SupplementaryTableS3.xlsx](#)
- [SupplementaryFigureLegends.docx](#)
- [SupplementaryFigureS1S5.pdf](#)